Spatial optimal disturbances of three-dimensional aerodynamic boundary layers [1)]

A. V. Boiko[a], K. V. Demyanko[a], S. A. Kusnetsova[a], Yu. M. Nechepurenko[a,*], G.V. Zasko[a]

[*] *Marchuk Institute of Numerical Mathematics, Russian Academy of Sciences, Gubkin str., 8, Moscow, Russia, 119333*

[*] *e-mail: yumnech@yandex.ru*

In the present paper, we propose a numerical method for modeling the downstream propagation of optimal disturbances in compressible boundary layers over three-dimensional aerodynamic configurations. At each integration step, the method projects the numerical solution of governing equations onto an invariant subspace of physically relevant eigenmodes; and the numerical integration is performed along the lines of disturbance propagation. The propagation of optimal disturbances is studied in a wide range of parameters for two configurations: a boundary layer over a swept wing of finite span, and a boundary layer over a prolate spheroid. It is found that the dependence of the disturbance energy amplification on the spanwise wavenumber has two local maxima. It is discussed how to combine the developed method with the modern approaches, which are designed to predict the onset of laminar–turbulent transition using the e^N-method.

Keywords: compressible boundary layers, spatial optimal disturbances, bypass transition, boundary layer over a swept wing, boundary layer over a prolate spheroid, e^N-method

DOI: 10.31857/S00444669250112e6

1. Introduction

One of the possible scenarios of the laminar–turbulent transition is the so-called bypass scenario, which is accompanied by the development of quasi-stationary disturbances dominated by the streamwise velocity component. Such disturbances are called streaks or streaky structures. Usually, the bypass scenario takes place at a high degree of the freestream turbulence.

The streaks develop from streamwise vortices due to the lift-up effect [1]–[3]. The lift-up effect is one of the main physical mechanisms responsible for a disturbance energy growth at finite time (or space) intervals [4]. Mathematically, this phenomenon is caused by the

[1)]The work is supported by Russian Science Foundation (Grant No. 22–11–00025).

non-orthogonality of eigenmodes of the linearized system governing the small-amplitude disturbance propagation [5]. For some specific disturbances, the transient energy growth might be of significant magnitude. The disturbance achieving maximum energy amplification at finite time intervals is called an optimal disturbance [6]–[9]. In particular, the optimal disturbances allow estimating various disturbance characteristics within the bypass scenario [10].

Spatial, both stationary and traveling, optimal disturbances of incompressible laminar boundary layers were first computed for the Blasius boundary layer [10, 11]. In these studies, it is taken into account that the main flow is non-parallel, i.e. the boundary layer thickness increases downstream. The spatial optimal disturbances are found for the Poiseuille flow in a circular pipe [12] and a plane channel [13], and for the boundary layer over a weakly concave surface [14]. In addition, optimal disturbances are studied for viscous incompressible jets [15, 16]. For compressible boundary layers, the spatial optimal disturbances were first computed in the work [17], with the local-parallel approximation being applied. For all these main flows with the disturbance parameters ensuring that any individual eigenmode decays downstream, it is shown that the maximum energy amplification is achieved by stationary vortices either periodic in spanwise direction or periodic in azimuthal direction (for the circular-pipe flow). The downstream propagation of optimal disturbances is studied both for the incompressible Falkner–Skan–Cooke boundary layer [18] and the compressible boundary layer with local self-similarity [19]. In these studies, non-parallel boundary layers are considered as well, and a variant of PSE method is used for describing the downstream propagation of disturbances. At parameter values ensuring the main boundary-layer linear instability, it is shown that the energy growth of optimal disturbances might exceed the growth predicted for modal instabilities by several orders of magnitude. In addition, the maximum energy amplification is achieved by traveling disturbances.

In the most studies mentioned above, the downstream propagation of small-amplitude disturbances is governed by equations, where the streamwise viscous dissipation terms as well as the streamwise pressure gradient are regarded as negligible. The equations thus obtained are parabolic, and the streamwise initial-value problem is well-posed for them. There is another approach, which does not require neglecting these terms in original equations. Namely, for modeling the downstream propagation of disturbances, one can project the numerical solution onto a subspace of physically relevant eigenmodes. This idea [17] is developed [20, 21, 22] by the authors, who use the abbreviation OWNS (One-Way

spatial integration of the Navier–Stokes equations) for this class of numerical methods. In the present paper, we use an original implementation of this approach, where the spectral projector [23] is computed at each integration step to exclude the contribution of non-physical modes. The non-physical modes are defined as those propagating upstream and growing downstream at large rates [24]. This method was tested for the downstream propagation of both Tollmien–Schlichting waves and Goertler vortices in the non-parallel boundary layer over a slightly concave plate [25, 24].

In all the above-mentioned studies, the non-modal stability analysis is performed for canonical main flows, which depend either on one or two spatial coordinates. The present paper aims at the development of an approach for the non-modal stability analysis of compressible boundary layers over three-dimensional aerodynamic configurations. This approach can be served as a basis for predicting the onset of the bypass laminar–turbulent transition in engineering applications. In addition, the paper discusses how to integrate this approach into a modern technology of the transition prediction by the e^N-method with the example of such a technology proposed in the work [26]. By the developed approach, we compute the spatial optimal disturbances for two three-dimensional aerodynamic configurations: a boundary layer over a swept wing of finite span, and a boundary layer over a prolate spheroid. Such a computation is done for the first time.

Over the last ten years, the authors of the present paper have been developing LOTRAN [26, 27], a software package designed for computing the position of the laminar–turbulent transition for three-dimensional aerodynamic boundary layers over flow-exposed bodies of small curvature. LOTRAN is widely used both for fundamental scientific research and for engineering purposes [28, 29, 30, 31, 26]. The coupling structure of LOTRAN is presented in Fig. 1.

LOTRAN is designed to work together with any CFD-code that computes a laminar–turbulent flow over a given flow-exposed body, using some turbulence model (e.g., k-ω SST [32]) and a given intermittency distribution. To compute the transition position, an iterative process starts. At each iteration, the laminar–turbulent flow is computed by CFD-code, with zero intermittency being set for the assumed laminar domain (and slightly downstream) and unit intermittency being set elsewhere. The obtained laminar–turbulent flow data, such as velocity components, pressure, temperature, and intermittency, are taken as an input for the *Main Flow* module; this module interpolates the data from the CFD-code grid to a tetrahedral grid. Next, the *Boundary Layer* module constructs 2D-slices along disturbance propagation lines in the domain of interest on the body surface.

The procedure for constructing the slices is described in detail in the work [26]. Then, this module introduces curvilinear orthogonal coordinates along the slices, constructing a computational grid within these coordinates and interpolating the flow data to that grid from the previous tetrahedral grid. Then, for each slice, the *Stability Analysis* module computes the neutral stability curves as well as the growth rates of the most unstable local modes being harmonic in time and spanwise coordinate. The downstream propagation of small-amplitude disturbances is governed by the viscous compressible heat-and-mass-transfer equations linearized with respect to the main flow [27]. These equations are briefly described in Section 2 of the present paper. Then, along each slice, the *Transition Analysis* module finds the transition onset by the e^N-method and evaluates the transition length. These results are given to the CFD-code to set a new intermittency distribution, and hence compute a new laminar–turbulent flow. Such an iterative process stops when the transition position converges with an acceptable accuracy.

Section 3 describes a numerical method for computing the spatial optimal disturbances of three-dimensional boundary layers. A new module, *Non-Modal Analysis*, implements this method within LOTRAN. The optimal disturbances are computed along the same slices as for the modal analysis. To this end, we numerically solve streamwise initial-value problems for the same small-amplitude disturbance propagation equations as within the modal analysis, while the original method [25, 24] is used for the numerical integration. As a result of the numerical integration with different initial values, we find the matrix of fundamental solutions. This matrix allows computing the spatial optimal disturbances, using the discrete analogue of the total energy density functional [17, 33].

Each slice consists of a few surface normals with the main flow data. These normals are called main normals. The distance between the adjacent main normals approximately equals the streamwise size of grid cells, which are used for the main-flow computation. However, such a distance is usually not small enough to be chosen as the streamwise integration step for modeling the downstream propagation of disturbances. Therefore, we introduce additional uniform grids between the main normals assuming that the main flow does not change between the adjacent main normals. The matrix of fundamental solutions between any two main normals is obtained by the multiplication of those between the adjacent main normals. This allows us to naturally parallelize the algorithm as well as to reduce the computational cost of parametric computations. Specifically, if all matrices of fundamental solutions between the adjacent main normals are found, then the optimal disturbances might be found efficiently for given pair of generation and observation points.

Section 4 shows the results of numerical experiments with the proposed numerical method and the two above-mentioned configurations. In the range of spanwise wavenumbers favorable for the development of crossflow vortices, it is shown that the energy amplification has an additional local maximum with the spanwise wavenumber being small. This phenomenon was previously observed in the laboratory experiments [34] for a swept wing, but was not confirmed numerically. For a prolate spheroid, this effect has not previously been found either experimentally or numerically. Section 5 summarizes the results of the present paper.

Throughout the present paper, $\|.\|_2$ denotes the 2-norm for vectors and matrices, I denotes the identity matrix whose order is clear from the context, and $'*'$ denotes the symbol of conjugate transposition.

2. Governing equations

In the Cartesian coordinates (x_1, x_2, x_3), let us consider the non-dimensional governing equations of viscous compressible media, which represent the conservation law of momentum, energy and mass, and the ideal gas law. Written with the tensor summation convention, these equations are as follows

$$\begin{aligned}
\rho\left(\frac{\partial u_i}{\partial t}+u_j\frac{\partial u_i}{\partial x_j}\right) &= -\frac{1}{\gamma M^2}\frac{\partial p}{\partial x_i}+\frac{1}{Re}\frac{\partial \sigma_{ij}}{\partial x_j},\\
\rho\left(\frac{\partial T}{\partial t}+u_j\frac{\partial T}{\partial x_j}\right) &= -(\gamma-1)\rho T\frac{\partial u_j}{\partial x_j}+\frac{\gamma}{PrRe}\frac{\partial}{\partial x_j}\left(\kappa\frac{\partial T}{\partial x_j}\right)+\gamma(\gamma-1)\frac{M^2}{Re}\Pi,\\
\frac{\partial \rho}{\partial t}+\frac{\partial(\rho u_j)}{\partial x_j} &= 0,\\
p &= \rho T,
\end{aligned} \tag{2.1}$$

where

$$\sigma_{ij}=2\mu e_{ij}+\lambda e_{kk}\delta_{ij},\quad e_{ij}=\frac{1}{2}\left(\frac{\partial u_i}{\partial x_j}+\frac{\partial u_j}{\partial x_i}\right),\quad \Pi=\sigma_{ij}e_{ij}.$$

Here u_j are the velocity components, ρ is the density, p is the static pressure, T is the temperature, μ and λ are the first and second viscosity coefficients, κ is the thermal conductivity, and γ is the adiabatic index. The Prandtl number, Mach number and Reynolds number are defined as

$$Pr=\frac{c_p\mu_{\text{ref}}}{\kappa_{\text{ref}}},\quad M=\frac{U_{\text{ref}}}{\sqrt{\gamma RT_{\text{ref}}}},\quad Re=\frac{U_{\text{ref}}L_{\text{ref}}\rho_{\text{ref}}}{\mu_{\text{ref}}}, \tag{2.2}$$

where the specific gas constant is denoted by R, and the specific heat at constant pressure by c_p. Here the subscript ref refers to dimensional scales, with L_{ref} and U_{ref} denoting

referential length and velocity scales. We assume that both the dynamic viscosity $\mu = \mu(T)$ and the heat conductivity $\kappa = \kappa(T)$ in (2.1) depend only on temperature, with these dependencies being given explicitly [35, 27]. For the second viscosity coefficient, the Stokes hypothesis $\lambda = -2\mu/3$ is assumed.

Suppose the system (2.1) has a stationary solution with the velocity components $\bar{u}_i$, temperature $\bar{T}$, density $\bar{\rho}$, pressure $\bar{p}$, and the coefficients $\bar{\mu} = \mu(\bar{T})$, $\bar{\lambda} = \lambda(\bar{T})$ and $\bar{\kappa} = \kappa(\bar{T})$. In the sequel, such a stationary solution is called the main flow. The propagation of small-amplitude disturbances against the main flow is governed by the following linearized equations [27]

$$
\begin{aligned}
&\bar{\rho}\left(\frac{\partial u_i'}{\partial t} + \bar{u}_j\frac{\partial u_i'}{\partial x_j} + u_j'\frac{\partial \bar{u}_i}{\partial x_j}\right) + \rho'\bar{u}_j\frac{\partial \bar{u}_i}{\partial x_j} = -\frac{1}{\gamma M^2}\frac{\partial p'}{\partial x_i} + \frac{1}{Re}\frac{\partial \sigma_{ij}'}{\partial x_j},\\
&\bar{\rho}\left(\frac{\partial T'}{\partial t} + \bar{u}_j\frac{\partial T'}{\partial x_j} + u_j'\frac{\partial \bar{T}}{\partial x_j}\right) + \rho'\bar{u}_j\frac{\partial \bar{T}}{\partial x_j} =\\
&-(\gamma-1)\left(\bar{\rho}\left(\bar{T}\frac{\partial u_j'}{\partial x_j} + T'\frac{\partial \bar{u}_j}{\partial x_j}\right) + \rho'\bar{T}\frac{\partial \bar{u}_j}{\partial x_j}\right) +\\
&\frac{\gamma}{PrRe}\frac{\partial}{\partial x_j}\left(\bar{\kappa}\frac{\partial T'}{\partial x_j} + \bar{\kappa}_T T'\frac{\partial \bar{T}}{\partial x_j}\right) + \gamma(\gamma-1)\frac{M^2}{Re}\Pi',\\
&\frac{\partial \rho'}{\partial t} + \frac{\partial \bar{\rho}u_j'}{\partial x_j} + \frac{\partial \rho'\bar{u}_j}{\partial x_j} = 0,\\
&p' = \bar{\rho}T' + \rho'\bar{T},
\end{aligned}
\tag{2.3}
$$

where

$$
\begin{aligned}
&\sigma_{ij}' = 2\bar{\mu}e_{ij}' + 2\bar{\mu}_T T'\bar{e}_{ij} + \left(\bar{\lambda}e_{kk}' + \bar{\lambda}_T T'\bar{e}_{kk}\right)\delta_{ij},\\
&e_{ij}' = \frac{1}{2}\left(\frac{\partial u_i'}{\partial x_j} + \frac{\partial u_j'}{\partial x_i}\right),\\
&\Pi' = \bar{\sigma}_{ij}e_{ij}' + 2\bar{\mu}e_{ij}'\bar{e}_{ij} + 2\bar{\mu}_T T'\bar{e}_{ij}\bar{e}_{ij} + \left(\bar{\lambda}e_{kk}'\bar{e}_{ij} + \bar{\lambda}_T T'\bar{e}_{kk}\bar{e}_{ij}\right)\delta_{ij}.
\end{aligned}
$$

Here the disturbance velocities are denoted by u_i', the disturbance temperature by T', the disturbance density by ρ', the disturbance pressure by p', and $\bar{f}_T = df/dT(\bar{T})$.

Within LOTRAN, the modal stability analysis is performed for laminar boundary layers over surfaces of small curvature. The disturbance propagation is studied along the boundary-layer slices (see Introduction), where the following curvilinear orthogonal coordinates are used: y is the distance to the surface along the normal, x is the arc length from the beginning of the slice to the base of this normal along the slice, and z is the spanwise coordinate. The main flow is assumed to be computed by a CFD-code. As for the referential dimensional scales in (2.2), we use those of the freestream. The dimensionless numbers (2.2) thus defined are denoted by Pr_∞, M_∞ and Re_∞.

We assume that the main flow does not depend on z along the slice, and hence only disturbances of the form

$$\mathrm{Real}\{\boldsymbol{\phi}\mathrm{e}^{\mathrm{i}(\beta z-\omega t)}\}, \tag{2.4}$$

are considered, where ω is the angular frequency, β is the spanwise wavenumber, and t is the time. Here $\boldsymbol{\phi}$ is the complex-valued vector of disturbance amplitudes that consists of the streamwise, normal and spanwise velocities, the pressure, and the temperature; and these amplitudes depend only on x and y. We also assume that the surface curvature is small, and the normal velocity of the main flow is negligible. In addition, we apply the local-parallel approximation, i.e. the main-flow components depend on x, but their derivatives on x are regarded as negligible.

Based on (2.3) but under the above-mentioned assumptions, one can derive [27] the equations governing the propagation of disturbance amplitudes of the form (2.4). In the present paper, we use these equations, with the disturbance amplitudes satisfying zero boundary conditions at $y = 0$ and $y = \infty$.

Optimal disturbances are computed along the boundary-layer slices, assuming that the disturbances are of the form (2.4). The downstream propagation of the optimal disturbances is governed by the same equations [27] as for the modal stability analysis.

3. Non-modal analysis

The governing equations, which are discussed in Section 2, are approximated in the normal direction y by a collocation method. Then, the disturbance amplitudes become vector functions depending only on x; and we keep the same notation for the disturbance amplitudes both before and after the spatial approximation. After the approximation, the disturbance amplitudes satisfy the system of ordinary differential equations [27]

$$\mathrm{A}\frac{d^2\boldsymbol{\phi}}{dx^2} + \mathrm{B}\frac{d\boldsymbol{\phi}}{dx} + (\mathrm{i}\omega\mathrm{C} - \mathrm{D})\,\boldsymbol{\phi} = 0. \tag{3.5}$$

Here A, B, C and D are square x-dependent matrices of order $5n_y$, where n_y is the number of the interior grid nodes in the normal direction. It is worth noting that A is a diagonal matrix whose last n_y diagonal entries are zero, and C is a nearly-diagonal matrix. Let us introduce four additional variables that represent the derivatives with respect to x of the disturbance velocity components and temperature. Then, equation (3.5) might be rewritten as the system of first-order ordinary differential equations

$$\mathrm{M}(x)\frac{d\mathbf{q}}{dx} = \mathbf{q}, \tag{3.6}$$

where $\mathrm{M}(x)$ is an x-dependent matrix of order $9n_y$, and $\mathbf{q} = \mathbf{q}(x)$ is a $9n_y$-component vector function.

Optimal disturbances largely depend on a functional, which is used for the optimization [36]. In the studies [33, 17, 19] of optimal disturbances of compressible boundary layers, the functional

$$\mathcal{E} = \int_0^{+\infty} \bar{\rho}\left(|u|^2 + |v|^2 + |w|^2\right) + \frac{\bar{T}}{\gamma M_\infty^2 \bar{\rho}}|\rho|^2 + \frac{\bar{\rho}}{\gamma(\gamma-1)M_\infty^2 \bar{T}}|T|^2\, dy \tag{3.7}$$

of total disturbance energy density is used, where u is the streamwise velocity amplitude, v is the normal velocity amplitude, w is the spanwise velocity amplitude, ρ is the density amplitude, and T is the temperature amplitude. Note that both the main-flow density $\bar{\rho}$ and the main-flow temperature $\bar{T}$ depend both on y and x, in general. Within LOTRAN, the disturbance pressure p appears in the governing equations instead of the disturbance density ρ. Using the relation

$$p = \bar{\rho}T + \bar{T}\rho \tag{3.8}$$

that comes from the ideal gas law, the discrete analogue of (3.7) might be rewritten as $\mathbf{q}^*\mathrm{E}\mathbf{q}$, where $\mathrm{E} = \mathrm{E}(x)$ is an x-dependent Hermitian matrix of rank $5n_y$.

3.1. Downstream integration

Each slice consists of a few main normals with the main flow data. We introduce additional uniform grids between the main normals with the same number of interior grid nodes n_x; and it is assumed that the main flow does not change between the adjacent main normals. The streamwise coordinates of the main normal bases are denoted by $x_1 < x_2 < \ldots$, the subgrid step by $h_j = (x_{j+1} - x_j)/(n_x + 1)$, and the subgrid nodes by $x_{j,k} = x_j + (k-1)h_j$.

Consider the streamwise initial-value problem for the system (3.6) with the initial node x_j, the final node x_{j+1}, and the initial condition $\mathbf{q}(x_j) = \mathbf{q}_j$. At x_j, we compute the system matrix $\mathrm{M}_j = \mathrm{M}(x_j)$ and use it at each integration step. The initial-value problem allows for non-physical solutions growing downstream at large rates and propagating upstream [17]. To exclude such solutions, we use standard numerical schemes combined with the spectral projection such as that for viscous incompressible flows [25, 24]. We project the numerical solution onto an invariant subspace of M_j corresponding to the physically relevant subset Λ_j of its spectrum.

The subset Λ_j consists of all eigenvalues λ satisfying the inequality Real $1/\lambda \leq 0.8\,|\beta|$, where β is the spanwise wavenumber [26]. This estimation is based on considering the asymptotic behavior of the branches of continuous spectrum of the problem [17]. It can be shown analytically that for the part of continuous spectrum in the right half-plane (corresponding to the upstream traveling disturbances) Imag$(1/\lambda) \geqslant |\beta|$. The coefficient 0.8 is introduced just to be on the safe side to guarantee that no upstream traveling mode is present in Λ_j. Note that in the cases under consideration linear instability occurs only at quite large values of $|\beta|$. Meanwhile, as our tests showed, the leading discrete mode always has Real $1/\lambda \leq 0.8\,|\beta|$. Outside of the linear instability region the inequality can be changed to Real $1/\lambda \leq 0$. Numerical experiments show that the physically relevant eigenvalues thus defined are well separated from the non-physical ones [24].

The spectral projectors at each j are computed using the Schur decomposition [37] of M_j. The spectral projector thus computed appears as $\mathrm{P}_j = \mathrm{X}_j\mathrm{Y}_j$ [23], where X_j is a rectangular matrix whose columns form the orthonormal basis in the invariant subspace of M_j corresponding to the subset Λ_j, and Y_j is a rectangular matrix ensuring the following identities

$$\mathrm{X}_j\mathrm{Y}_j\mathrm{M}_j = \mathrm{X}_j\mathrm{S}_j\mathrm{Y}_j = \mathrm{M}_j\mathrm{X}_j\mathrm{Y}_j,\ \mathrm{Y}_j\mathrm{X}_j = \mathrm{I}$$

being valid, where $\mathrm{S}_j = \mathrm{X}_j^*\mathrm{M}_j\mathrm{X}_j$ is the restriction of M_j to the invariant subspace.

At the first integration step we use the implicit Euler method modified as follows

$$\tilde{\mathbf{q}}_{j,1} = \mathrm{Y}_j\mathbf{q}_j,\ \mathrm{S}_j\frac{\tilde{\mathbf{q}}_{j,2} - \tilde{\mathbf{q}}_{j,1}}{h_j} = \tilde{\mathbf{q}}_{j,2},$$

where $\mathbf{q}_j$ is the solution at the j-th main normal. At other integration steps, we use the BDF-2 scheme modified as follows

$$\mathrm{S}_j\frac{3\tilde{\mathbf{q}}_{j,k} - 4\tilde{\mathbf{q}}_{j,k-1} + \tilde{\mathbf{q}}_{j,k-2}}{2h_j} = \tilde{\mathbf{q}}_{j,k}.$$

After the last step done, we put $\mathbf{q}_{j+1} = \mathrm{P}_{j+1}\mathrm{X}_j\tilde{\mathbf{q}}_{j,n_x+2}$.

To compute the matrix of fundamental solutions Φ_j between normals j and $j+1$, we take the columns of the identity matrix as the initial condition $\tilde{\mathbf{q}}_{j,1}$. Then, the columns of Φ_j are the vectors $\tilde{\mathbf{q}}_{j,n_x+2}$, with the matrix Φ_j satisfying the equality $\mathbf{q}_{j+1} = \mathrm{P}_{j+1}\mathrm{X}_j\Phi_j\mathrm{Y}_j\mathbf{q}_j$ for any initial condition $\mathbf{q}_j$. Thus, one can represent the numerical solution of the streamwise initial-value problem between the j_g-th and j_o-th main normals as

$$\mathrm{q}_{j_o} = \mathrm{P}_{j_o}\mathrm{X}_{j_o-1}\Phi_{j_o-1}\mathrm{Y}_{j_o-1}\ldots\mathrm{X}_{j_g}\Phi_{j_g}\mathrm{Y}_{j_g}\mathrm{q}_{j_g} = \mathrm{X}_{j_o}\mathrm{F}_{j_g,j_o}\mathrm{Y}_{j_g}\mathrm{q}_{j_g},$$

where

$$\mathrm{F}_{j_g,j_o} = \mathrm{Y}_{j_o}\mathrm{X}_{j_o-1}\Phi_{j_o-1}\ldots\mathrm{Y}_{j_g+1}\mathrm{X}_{j_g}\Phi_{j_g}.$$

3.2. Computation of optimal disturbances

We say that the optimal disturbance is a disturbance being generated at $x = x_{j_g}$ and achieving the maximum energy amplification at $x = x_{j_o}$. In the sequel, x_{j_g} is called the generation point, and x_{j_o} is called the observation point. In addition, we suppose that the optimal disturbance belongs to an invariant subspace of physically relevant eigenmodes of a given dimension m. This invariant subspace is constructed in two steps. First, we select the subset Λ_{j_g} of the spectrum of M_{j_g}, as described above. Next, among the eigenvalues of Λ_{j_g}, we select m ones having the largest values of Real $1/\lambda$ and use the obtained set instead of Λ_{j_g}, keeping the same notation. Since the rank of the matrix $\mathrm{E}(x)$ is equal to $5n_y$, then m should not exceed $5n_y$. For numerical experiments, we choose $m = 2n_y$, since for a fixed number of grid nodes n_y, the maximum disturbance energy amplification converges with further increase in m.

The optimal disturbance is computed by solving the problem that consist in maximizing the energy amplification of disturbances from the subspace associated with Λ_{j_g}:

$$\max_{\mathbf{q}_{j_g}=\mathrm{P}_{j_g}\mathbf{q}_{j_g}\neq 0} \frac{\mathbf{q}_{j_o}^* \mathrm{E}_{j_o} \mathbf{q}_{j_o}}{\mathbf{q}_{j_g}^* \mathrm{E}_{j_g} \mathbf{q}_{j_g}}, \tag{3.9}$$

where $\mathrm{E}_j = \mathrm{E}(x_j)$.

By L_j denote the lower triangular matrix that forms the factorization $\mathrm{E}_j = \mathrm{L}_j^* \mathrm{L}_j$. Let $\mathrm{L}_j \mathrm{X}_j = \mathrm{Q}_j \mathrm{R}_j$ be the QR-decomposition [37] with the unitary rectangular matrix Q_j and the upper triangular matrix R_j. Let $\tilde{\mathbf{q}}_j = \mathrm{Y}_j \mathbf{q}_j$ and $\boldsymbol{\mu}_j = \mathrm{R}_j \tilde{\mathbf{q}}_j$. Then

$$\frac{\mathbf{q}_{j_o}^* \mathrm{E}_{j_o} \mathbf{q}_{j_o}}{\mathbf{q}_{j_g}^* \mathrm{E}_{j_g} \mathbf{q}_{j_g}} = \frac{\|\mathrm{L}_{j_o} \mathbf{q}_{j_o}\|_2^2}{\|\mathrm{L}_{j_g} \mathbf{q}_{j_g}\|_2^2} = \frac{\|\mathrm{L}_{j_o} \mathrm{X}_{j_o} \tilde{\mathbf{q}}_{j_o}\|_2^2}{\|\mathrm{L}_{j_g} \mathrm{X}_{j_g} \tilde{\mathbf{q}}_{j_g}\|_2^2} = \frac{\|\mathrm{R}_{j_o} \mathrm{F}_{j_g,j_o} \mathrm{R}_{j_g}^{-1} \boldsymbol{\mu}_{j_g}\|_2^2}{\|\boldsymbol{\mu}_{j_g}\|_2^2}.$$

Therefore, the solution of the problem (3.9) is reduced to computing the largest singular value of the matrix $\mathrm{R}_{j_o} \mathrm{F}_{j_g,j_o} \mathrm{R}_{j_g}^{-1}$ and the corresponding normalized right singular vector $\boldsymbol{\mu}_{j_g}^{\mathrm{opt}}$. The optimal disturbance in physical variables is then computed by the formula $\mathbf{q}_{j_g}^{\mathrm{opt}} = \mathrm{X}_{j_g} \mathrm{R}_{j_g}^{-1} \boldsymbol{\mu}_{j_g}^{\mathrm{opt}}$, and its downstream propagation is governed by the formula $\mathbf{q}_j^{\mathrm{opt}} = \mathrm{X}_j \mathrm{F}_{j_g,j} \mathrm{Y}_{j_g} \mathbf{q}_{j_g}^{\mathrm{opt}}$ for $j \geqslant j_g$. At the same time, the value

$$\mathcal{E}_j(x_{j_g}, x_{j_o}) = (\mathbf{q}_j^{\mathrm{opt}})^* \mathrm{E}_j \mathbf{q}_j^{\mathrm{opt}} = \|\boldsymbol{\mu}_j^{\mathrm{opt}}\|_2^2$$

is the total energy density of the optimal disturbance at a point $x = x_j$. For the point x_{j_o}, the maximum N-factor among disturbances generated at x_{j_g} is thus equal to

$$N_{\max}(x_{j_g}, x_{j_o}) = \frac{1}{2} \ln \mathcal{E}_j(x_{j_g}, x_{j_o}).$$

4. Results

This section discusses results of the computation of optimal disturbances for two configurations illustrated in Fig. 1 in the global Cartesian coordinates (X, Y, Z):

A) the windward surface of swept wing at an angle of attack of $-5°$. The wing has the modified NACA 67 1-215 laminarized airfoil with a chord length (normal to the leading edge) of 0.7 m, and 45° sweep angle. The freestream parameters are as follows: the velocity $U_\infty = 27$ m/s, the density $\rho_\infty = 1.18$ kg/m^3, and the kinematic viscosity $\nu_\infty = 1.57 \times 10^{-5}$ m^2/s. Such parameter values correspond to the Reynolds number $Re_\infty = 1.72 \times 10^6$ and the Mach number $M_\infty = 0.08$. This configuration corresponds to experiments [38, 39] on the laminar–turbulent transition in boundary layers over the swept wing SW-45 at various angles of attack. Data on the considered laminar boundary layer are computed [26, 40, 41] by ANSYS Fluent in a digital analogue of the test section of the T-324 wind tunnel of ITAM SB RAS.

B) prolate spheroid at an angle of attack of $+10°$. The spheroid has a length of 2.4 m, and an aspect ratio of $6 : 1 : 1$. The freestream parameters are as follows: the velocity $U_\infty = 45$ m/s, the density $\rho_\infty = 1.23$ kg/m^3, and the kinematic viscosity $\nu_\infty = 1.50 \times 10^{-5}$ m^2/s. Such parameter values correspond to the Reynolds number $Re_\infty = 7.20 \times 10^6$ and the Mach number $M_\infty = 0.13$. This configuration corresponds to experiments [42, 43] on the laminar–turbulent transition in boundary layers over bodies of revolution. Data on the considered laminar boundary layer are computed [26] using ANSYS Fluent.

The boundary layer stability is analyzed along the slices shown in Fig. 2. Profiles of the streamwise and spanwise velocity components of the main flow near the surface along these slices are shown in the local orthogonal coordinates in Fig. 3. The zero of the streamwise local coordinate x coincides with the beginning of the slice. The spanwise velocity is large enough (up to 7% of the streamwise velocity) for the development of vortices of the crossflow instability [44]. In the present paper, the stability of the boundary layers is studied at zero angular frequency and the values of the spanwise wavenumber typical to the development of stationary crossflow vortices. In all numerical experiments, we fix the disturbance generation point $x_{j_g} = 0$ as the beginning of the slice, with the observation point $x_{j_o} > 0$ being varied.

In the (x_{j_o}, β)-plane, Fig. 4 shows the level lines of the maximum N-factors, $N_{\max}(0, x_{j_o})$, of the optimal disturbances for both configurations, as well as the points at which a

growth of stationary crossflow vortices is observed. It is seen that for both configurations, the regions of modal and non-modal instability have a significant overlap. At the same time, at relatively small values of β and sufficiently large values of x_{j_o}, only the non-modal instability is observed, although it is characterized by relatively small maximum N-factors. This is further illustrated in Fig. 5, which shows the dependence of the maximum N-factors on $-\beta$ for a fixed x_{j_o}. It is seen that, in addition to the global maximum in the spanwise wavenumber, the dependence has a local maximum associated with the optimal disturbance that has a small spanwise wavenumber and does not contain modes growing downstream. For the boundary layer over the swept wing, the obtained result is in qualitative agreement with the experimental observation [34], while for that over the prolate spheroid this effect is discovered for the first time. Note that this effect suggests the possibility of bypass transition for the considered configurations.

Fig. 6 shows the dependence of the total energy density amplification of optimal disturbances on x computed for various observation points. Fig. 7 shows the absolute values of the disturbance velocity components. It is seen that at spanwise wavenumbers specific to the development of stationary crossflow vortices, the optimal disturbance weakly depends on the observation point. In addition, as it is seen from Fig. 8, the shape of the developed optimal disturbance is close to that of the leading local mode.

5. Conclusion

Using an original numerical method, we compute for the first time the downstream propagation of optimal disturbances for two three-dimensional aerodynamic configurations: a boundary layer over a finite-span swept wing, and a boundary layer over a prolate spheroid. The basis of this method is the projection of the solution to an initial-value problem, which governs the propagation of the disturbances, onto an invariant subspace of physically significant eigenmodes at each step of numerical integration along the selected lines of disturbance propagation.

In this work, the stability of the boundary layers was studied at zero angular frequency. It is shown that there are two maxima of the disturbance energy amplification in spanwise wavenumbers. One of them corresponds to the development of stationary vortices of the crossflow instability, and the other one, at lower values of the spanwise wavenumber, corresponds to the non-modal instability, previously observed in experiments on a swept wing.

Additionally, the presented examples show that the proposed method can serve as a basis for an engineering approach to the non-modal spatial stability analysis of various boundary layers. In particular, the proposed method is prospective for predicting the bypass laminar–turbulent transition within the framework of existing engineering approaches based on the modal stability analysis by the e^N-method.

Fig. 1: The coupling structure of LOTRAN, the software package used.

Fig. 2: The windward surface of the swept wing (top), the side surface of the prolate spheroid (bottom), and the slices along which the boundary layer stability is studied. The slices are formed by external normals (black) to the flow-exposed surface (gray) along the line of disturbance propagation, with the projection of that line onto the surface being shown in red.

Fig. 3: Streamwise (first column) and spanwise (second column) velocity of the main flow near the surface along the slice on the swept wing (top) and the prolate spheroid (bottom). Line colors correspond to values of the streamwise coordinate x.

Fig. 4: Level lines of the maximum N-factors, $N_{\max}(0, x_{j_o})$, of the optimal disturbances in the boundary layer along the slice on the swept wing (top) and the prolate spheroid (bottom) in the (x_{j_o}, β)-plane. The white points denote the values x_{j_o} and β at which the stationary crossflow vortices grow. The right column shows the results at small β.

Fig. 5: Dependence of the maximum N-factors, $N_{\max}(0, x_{j_o})$, of the optimal disturbances on $-\beta$ for a fixed observation point, x_{j_o}, in the boundary layer along the slice on the swept wing (left) and the prolate spheroid (right).

Fig. 6: Dependence on x of the total energy density amplification, $\mathcal{E}_j(x_{j_g}, x_{j_o})$, of the optimal disturbances corresponding to various observation points: $x_{j_o} = 0.09$ (red), $x_{j_o} = 0.30$ (green), and $x_{j_o} = 0.54$ (blue) for the swept wing (left) at $\beta = -1500$; and $x_{j_o} = 0.26$ (red), $x_{j_o} = 0.38$ (green), $x_{j_o} = 0.49$ (blue) for the prolate spheroid (right) at $\beta = -3000$.

Fig. 7: The absolute values of the velocity components of optimal disturbances corresponding to various observation points: $x_{j_o} = 0.09$ (red), $x_{j_o} = 0.30$ (green), and $x_{j_o} = 0.54$ (blue) for the swept wing (top) at $\beta = -1500$; and $x_{j_o} = 0.26$ (red), $x_{j_o} = 0.38$ (green), $x_{j_o} = 0.49$ (blue) for the prolate spheroid (bottom) at $\beta = -3000$.

Fig. 8: The absolute values of the velocity components of the developed optimal disturbance (solid) and the leading local mode (dashed) corresponding to various observation points: $x_{j_o} = 0.09$ (red), $x_{j_o} = 0.30$ (green), and $x_{j_o} = 0.54$ (blue) for the swept wing (top) at $\beta = -1500$; and $x_{j_o} = 0.26$ (red), $x_{j_o} = 0.38$ (green), and $x_{j_o} = 0.49$ (blue) for the prolate spheroid (bottom) at $\beta = -3000$.

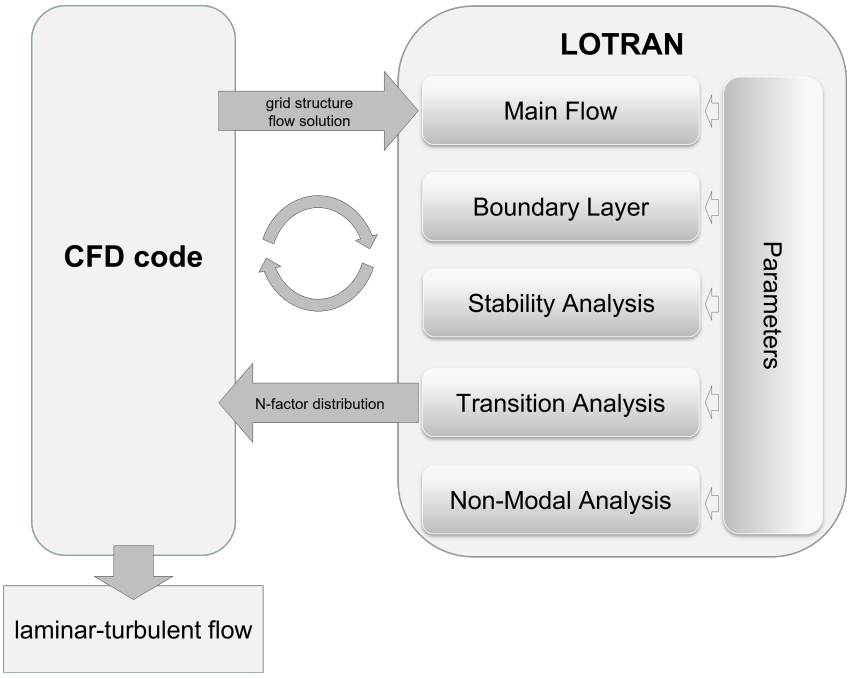
LOTRAN
CFD code
grid structure
flow solution
Main Flow
Boundary Layer
Stability Analysis
Transition Analysis
Non-Modal Analysis
Parameters
N-factor distribution
laminar-turbulent flow

Fig. 1

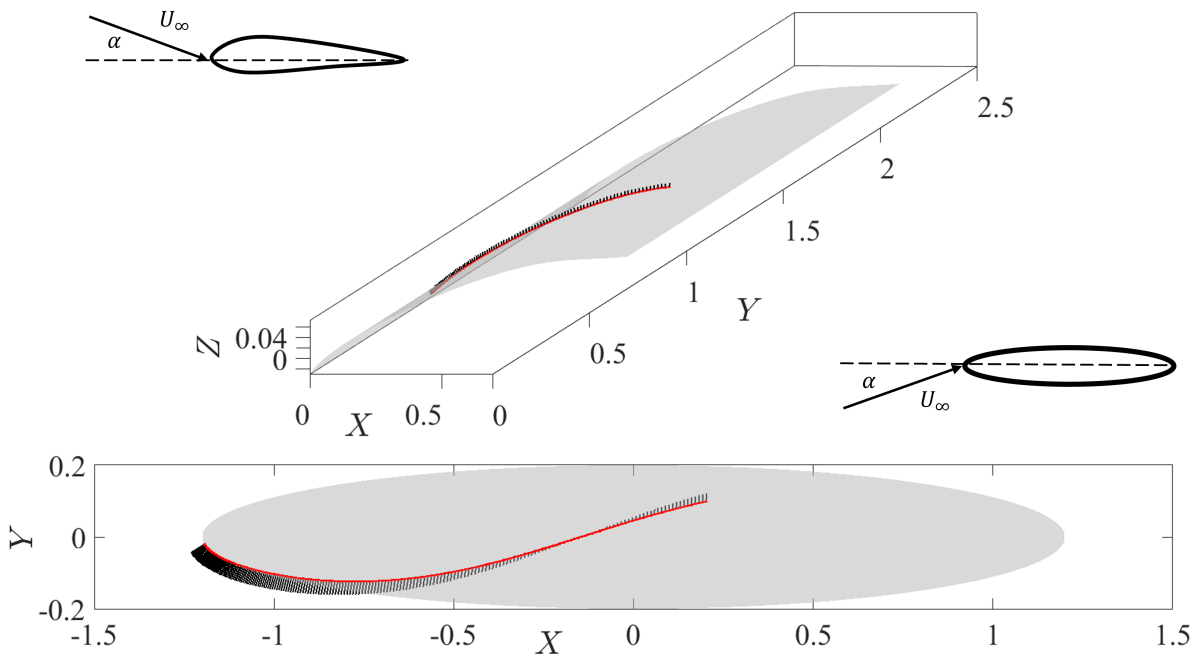
U_∞
α
2.5
2
1.5
1
0.5
Y
Z
0.04
0
0
X
0.5
0
α
U_∞
0.2
0
-0.2
Y
-1.5
-1
-0.5
X
0
0.5
1
1.5

Fig. 2

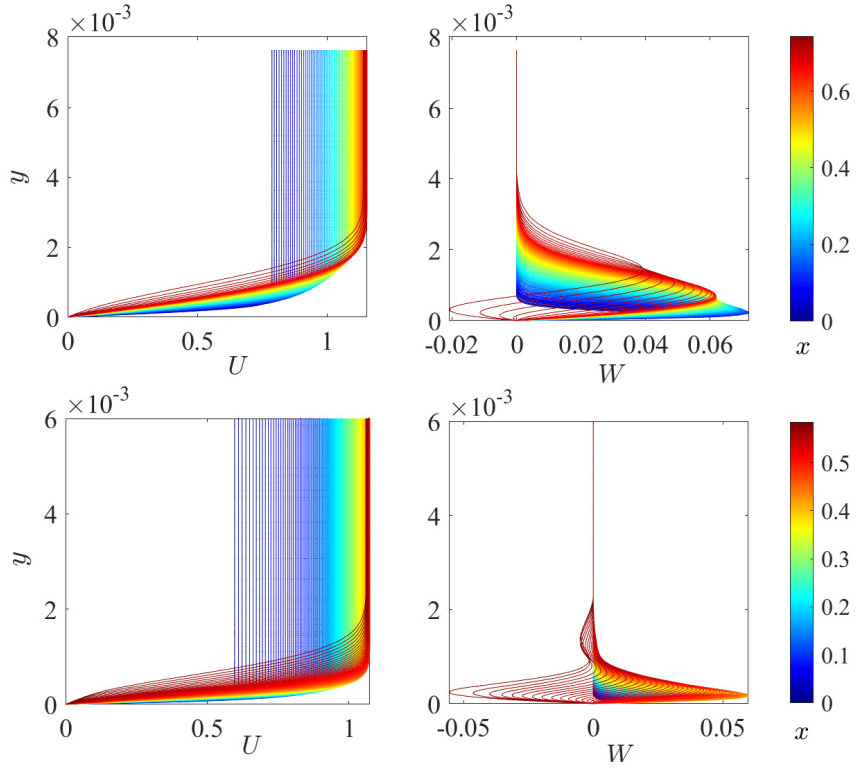
$\times 10^{-3}$
8
6
4
2
0
y
0
0.5
1
U
$\times 10^{-3}$
-0.02
0
0.02
0.04
0.06
W
0.6
0.4
0.2
0
x
$\times 10^{-3}$
6
4
2
0
y
0
0.5
1
U
$\times 10^{-3}$
-0.05
0
0.05
W
0.5
0.4
0.3
0.2
0.1
0
x

Fig. 3

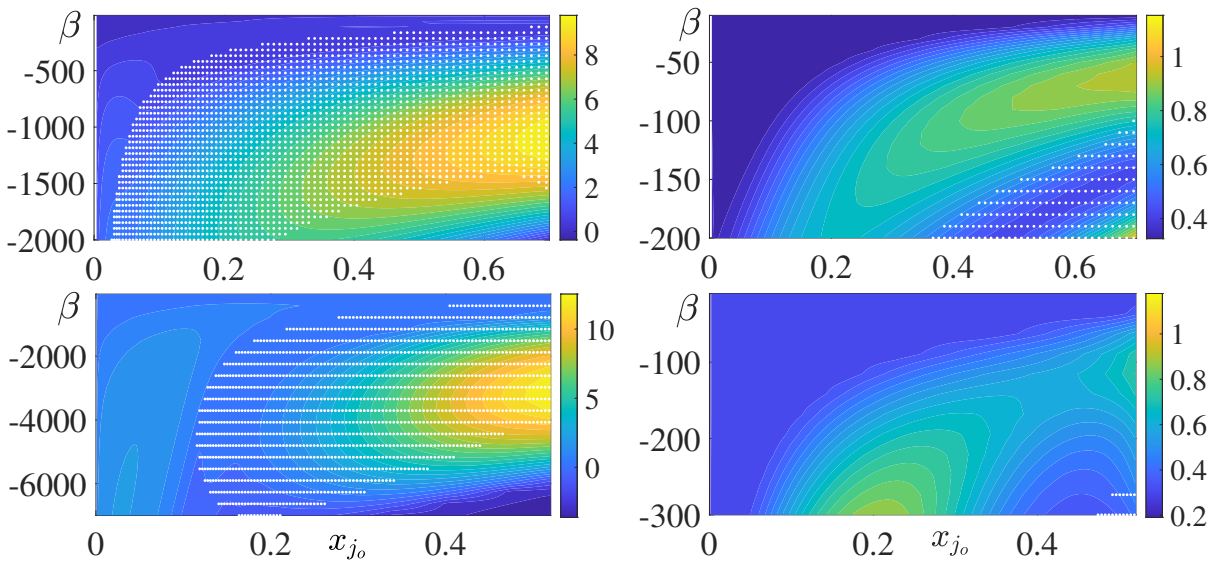

Fig. 4

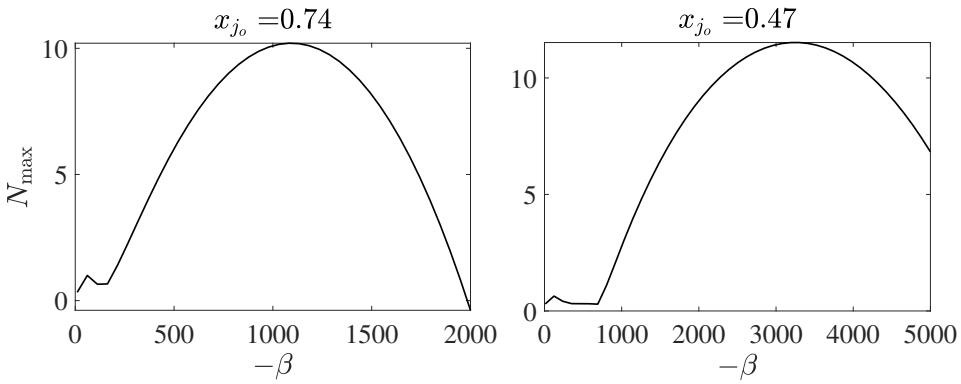

Fig. 5

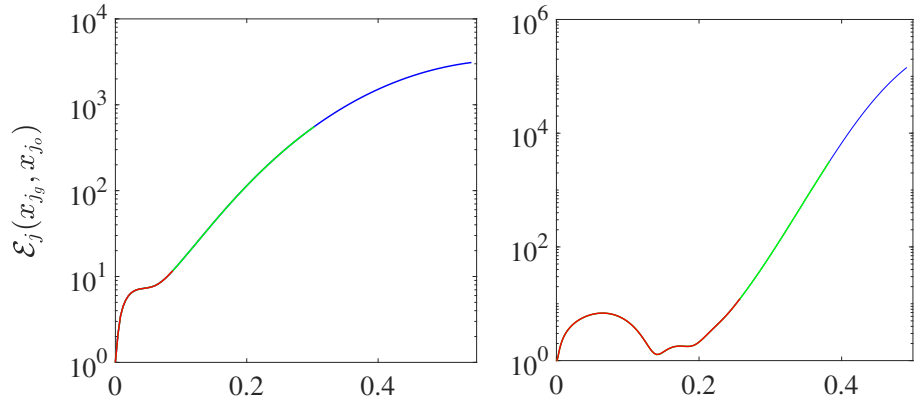

Fig. 6

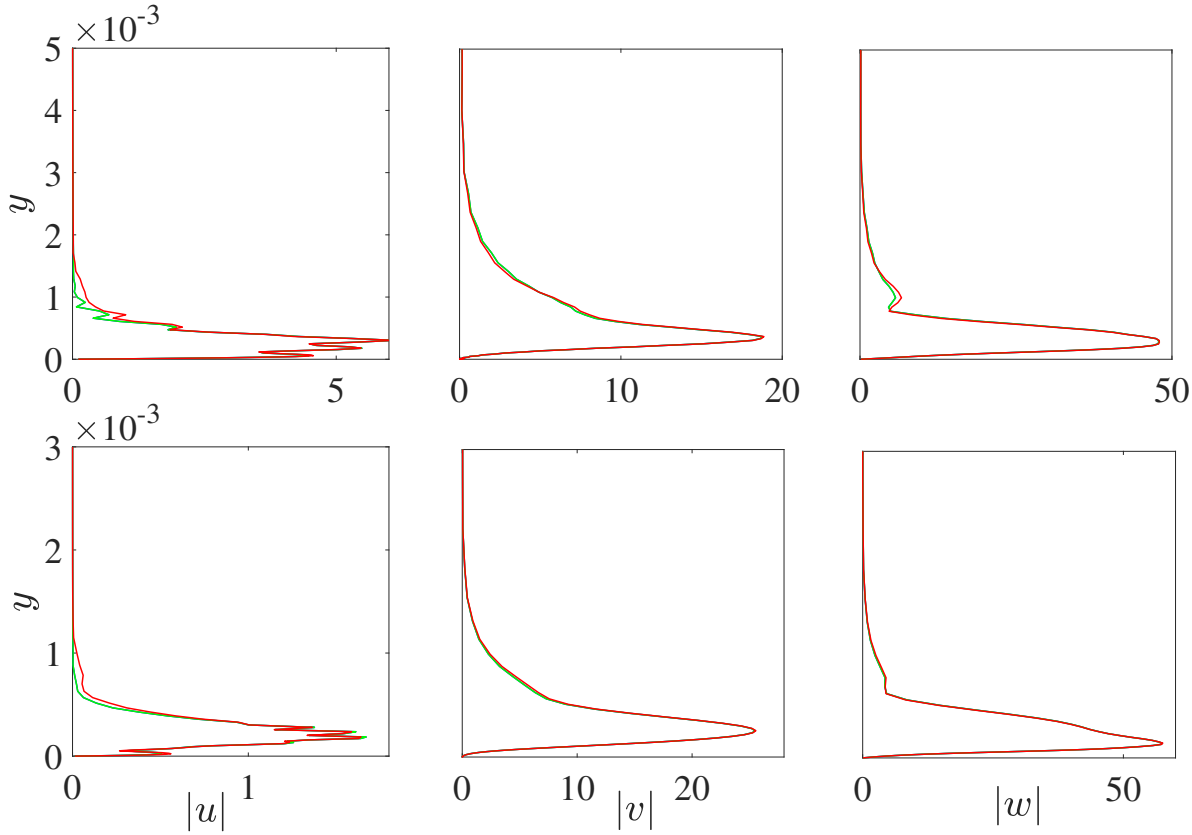

Fig. 7

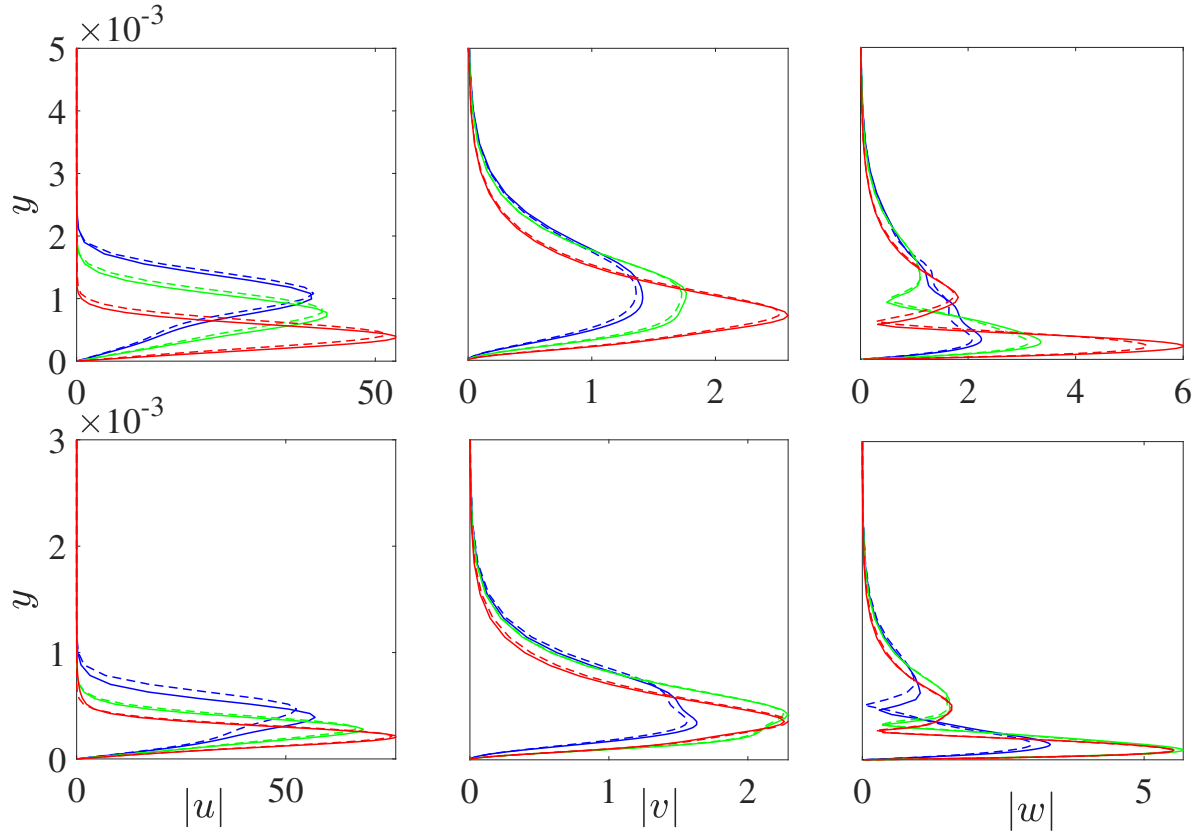

Fig. 8

Список литературы

[1] *Landahl M.T.* Wave breakdown and turbulence // SIAM J. Appl. Math. 1975. V. 28. в„– 4. P. 735–756.

[2] *Ellingsen T., Palm E.* Stability of linear flow // Phys. Fluids. 1975. V. 18. в„– 4. P. 487–488.

[3] *Landahl M.T.* A note on an algebraic instability of inviscid parallel shear flows // J. Fluid. Mech. 1980. V. 98. в„– 2. P. 243–251.

[4] *Brandt L.* The lift-up effect: the linear mechanism behind transition and turbulence in shear flows // Eur. J. Mech. B/Fluid. 2014. V. 47. P. 80–96.

[5] *Schmid P.J., Henningson D.S.* Stability and Transition in Shear Flows. Springer, 2001. 558 pp.

[6] *Farrell B.F.* The initial growth of disturbances in a baroclinic flow // J. Atmos. Sci. 1982. V. 39. P. 1663–1686.

[7] *Farrell B.F.* Optimal excitation of neutral Rossby waves // J. Atmos. Sci. 1988. V. 45. в„– 2. P. 163–172.

[8] *Farrell B.F.* Optimal excitation of baroclinic waves // J. Atmos. Sci. 1989. V. 46. в„– 9. P. 1193–1206.

[9] *Farrell B.F.* Optimal excitation of perturbations in viscous shear flow // Phys. Fluid. 1988. V. 31. в„– 8. P. 2093–2102.

[10] *Andersson P.A., Berggren M., Henningson D.S.* Optimal disturbances and bypass transition in boundary layers // Phys. Fluid. 1999. V. 11. в„– 1. P. 134–150.

[11] *Luchini P.* Reynolds-number-independent instability of the boundary layer over a flat surface: optimal perturbations // J. Fluid. Mech. 2000. V. 404. P. 289–309.

[12] *Reshotko E., Tumin A.* Spatial theory of optimal disturbances in a circular pipe flow // Phys. Fluid. 2001. V. 13. P. 991–996.

[13] *Biau D., Bottaro A.* Transient growth and minimal defects: Two possible initial paths of transition to turbulence in plane shear flows // Phys. Fluid. 2004. V. 16. в„– 10. P. 3515–3529.

[14] *Boiko A.V., Ivanov A.V., Kachanov Yu.S., Mischenko D.A., Nechepurenko Yu.M.* Excitation of unsteady Görtler vortices by localized surface nonuniformities // Theor. Comput. Fluid Dyn. 2017. V. 31. в„– 1. P. 67–88.

[15] *Boronin S.A., Healey J.J., Sazhin S.S.* Non-modal stability of round viscous jets // J. Fluid Mech. 2013. V. 716. P. 96–119.

[16] *Ivanov O.O., Ashurov D.A., Gareev L.R., Vedeneev V.V.* Non-modal perturbation growth in a laminar jet: An experimental study // J. Fluid Mech. 2023. V. 963. A8.

[17] *Tumin A., Reshotko E.* Spatial theory of optimal disturbances in boundary layers // Phys. Fluids. 2001. V. 13. P. 2097–2104.

[18] *Tempelmann D., Hanifi A., Henningson D.S.* Spatial optimal growth in three-dimensional boundary layers. // J. Fluid Mech. 2010. V. 646. P. 5–37.

[19] *Tempelmann D., Hanifi A., Henningson D.S.* Spatial optimal growth in three-dimensional compressible boundary layers. // J. Fluid Mech. 2012. V. 704. P. 251–279.

[20] *Towne A., Colonius T.* One-way spatial integration of hyperbolic equations // J. Comp. Phys. 2015. V. 300. P. 844–861.

[21] *Rigas G., Colonius T., Beyar M.* Stability of wall-bounded flows using one-way spatial integration of Navier-Stokes equations // 55-th AIAA Aerospace Sciences Meeting, Grapevine, Texas. AIAA Paper. 2017. в„– 2017–1881.

[22] *Zhu M., Towne A.* Recursive one-way Navier-Stokes equations with PSE-like cost // J. Comp. Phys. 2023. V. 473. P. 111744.

[23] *Godunov S.K.* Modern Aspects of Linear Algebra. American Mathematical Society, Providence, USA, 1998.

[24] **Zasko G.V., Boiko A.V., Demyanko K.V., Nechepurenko Yu.M.** Simulating the propagation of boundary-layer disturbances by solving boundary-value and initial-value problems // Russ. J. Numer. Anal. Math. Model. 2024. V. 39. в„– 1.

[25] *Boiko A.V., Demyanko K.V., Zasko G.V., Nechepurenko Yu.M.* On parabolization of equations governing small disturbances in 2D boundary layers // Thermophys. Aeromechanics. 2024. V. 31 (accepted).

[26] *Boiko A.I., Demyanko K.V., Kirilovskiy S.V., Nechepurenko Yu.M., Poplavskaya T.V.* Modeling of transonic transitional three dimensional flows for aerodynamic applications // AIAA J. 2021. V. 59. P. 1–13.

[27] *Boiko A.V., Demyanko K.V., Nechepurenko Yu.M.* On computing the location of laminar–turbulent transition in compressible boundary layers // Russ. J. Numer. Anal. Math. Model. 2017. V. 32. P. 1–12.

[28] *Boiko A.V., Demyanko K.V., Inozemtsev A.V., Kirilovskiy S.V., Nechepurenko Yu.M., Paduchev A.P., Poplavskaya T.V.* Determination of the Laminar–Turbulent Transition Location in Numerical Simulations of Subsonic and Transonic Flows Past a Flat Plate // Thermophys. Aeromechanics. 2019. V. 26. в„– 5. P. 629–637.

[29] *Kirilovskiy S.V., Boiko A.V., Demyanko K.V., Nechepurenko Yu.M., Poplavskaya T.V., Sidorenko A.A.* On integrating the LOTRAN 3.0 package into the ANSYS fluent CFD software. // AIP Conf. Proc. 2019. V. 2125. Art. 030098.

[30] *Poplavskaya T.V., Boiko A.V., Demyanko K.V., Kirilovskiy S.V., Nechepurenko Yu.M.* Numerical simulation of the transition to turbulence in subsonic and transonic flows // J. Phys.: Conf. Ser. 2019. V. 1359. Art. 012068.

[31] *Kirilovskiy S.V., Boiko A.V., Demyanko K.V., Ivanov A.V., Nechepurenko Yu.M., Poplavskaya T.V.* Numerical simulation of the laminar–turbulent transition on a swept wing in a subsonic flow // J. Phys.: Conf. Ser. 2019. V. 1359. Art. 012070.

[32] *Menter F.R.* Two-equation eddy-viscosity turbulence models for engineering applications // AIAA Journal. 1994. V. 32. P. 1598–1605.

[33] *Hanifi A., Schmid P.J., Henningson D.S.* Transient growth in compressible boundary layer flow // Phys. Fluid. 1996. V. 8. P. 826–837.

[34] *Boiko A.V.* Swept-Wing Boundary Layer Receptivity to a Steady Free-Stream Vortex Disturbance // Fluid Dynamics. 2002. V. 37. P. 37–45.

[35] *Mack L.M.* Boundary-layer Linear Stability theory // In AGARD Report No. 709: Special course on stability and transition of laminar flow. 1984. P. 3–81.

[36] *Schmid P.J.* Nonmodal stability theory // Ann. Rev. Fluid Mech. 2007. V. 39. P. 129–162.

[37] *Golub G.H., van Loan C.F.* Matrix Computations (4-th ed.). London: John Hopkins University Press. 2013. 784 p.

[38] *Ivanov A.V., Mischenko D.A., Boiko A.V.* Method of the description of the laminar-turbulent transition position on a swept wing in the flow with an enhanced level of free-stream turbulence // J. Appl. Mech. Tech. Phys. 2020. V. 61. P. 250–255.

[39] *Boiko A.V., Ivanov A.V., Borodulin V.I., Mischenko D.A.* Quantification technique of transition to turbulence in boundary layers using infrared thermography // Int. J. Heat Mass Transf. 2022. V. 183. P. 122065.

[40] *Boiko A.V., Demyanko K.V., Nechepurenko Yu.M., Zasko G.V.* On the use of probability-based methods for estimating the aerodynamic boundary-layer thickness // Fluid. 2021. V. 6. в„– 8. P. 267.

[41] *Kirilovskiy S.V., Boiko A.V., Demyanko K.V., Nechepurenko Yu.M., Poplavskaya T.V.* Simulation of the laminar-turbulent transition in the boundary layer of the swept wing in the subsonic flow at angles of attack // AIP Conf. Proc. 2020. V. 2288. P. 1–6.

[42] *Kreplin H.P., Vollmers H., Meier H.U.* Measurements of the wall shear stress on an inclined prolate spheroid // Z. Flugwiss. Weltraumforsch. 1982. V. 6. P. 248–252.

[43] *Meier H.U.* Experimental investigation of the boundary layer transition and separation on a body of revolution // Z. Flugwiss. Weltraumforsch. 1980. V. 4. P. 65–71.

[44] *Boiko A.V.* Receptivity of boundary layers to free stream axial vortices. DLR:Göttingen, Germany, 2000. IB 223–2000 A10. 60 p.